

# Entrainment and advection in an island's tidal wake, as revealed by light attenuation, zooplankton, and ichthyoplankton

*Iain M. Suthers*

School of Biological, Earth and Environmental Sciences, University of New South Wales, Sydney, New South Wales 2052, Australia

*C. T. Taggart and D. Kelley*

Department of Oceanography, Dalhousie University, Halifax, Nova Scotia B3H 4J1, Canada

*D. Rissik*

School of Biological, Earth and Environmental Sciences, University of New South Wales, Sydney, New South Wales 2052, Australia

*J. H. Middleton*

School of Mathematics, University of New South Wales, Sydney, New South Wales 2052, Australia

## *Abstract*

Spatial and temporal patterns of light attenuation, zooplankton abundance, and larval fish assemblages observed at night in the flood tide wake of a 2-km-wide, steep-sided island within the Great Barrier Reef lagoon (40–45-m local depth) are compared with two simple models. Eddy upwelling is shown to be slow relative to erosion, vertical entrainment, and advection (EA) arising near the flanks of the island, where currents were accelerated to 1–2 m s<sup>-1</sup>, approximately twice that in the free stream. Turbidity (particles <300- $\mu$ m equivalent spherical diameter [ESD], inferred from increased water column light attenuation of an optical plankton counter) and medium-sized zooplankton (700–1,000- $\mu$ m ESD) appeared to be entrained toward the surface, to form a V-shaped plume. The plume originated near the island's flanks and converged 4 km downstream. Here, light attenuation returned to the free stream conditions, presumably as sediments settled, leaving a patch of medium-sized zooplankton that had a three- to fourfold greater biomass concentration than the free stream. A decrease in the concentration of small zooplankton (300–500- $\mu$ m ESD, generally found in surface waters) is also consistent with vertical mixing by EA. Neuston net collections across the wake revealed two larval fish assemblages that were correlated with either the small surface zooplankton or with the deeper, medium-sized zooplankton, which included epibenthic taxa. If EA is a common process for patch formation in tidal waters, then the geometry of the associated plumes may predict larval settlement (recruitment “hotspots”) in shallow tidal waters.

Swirls of turbidity in the wakes of small islands are distinctive features within shallow, tidally energetic areas such as the Great Barrier Reef lagoon (Hamner and Hauri 1977; Wolanski et al. 1984*a,b*). Wakes of this nature may extend downstream several island diameters within the semidiurnal tidal excursion, and they may exist for periods of 4–5 h (Black and Gay 1986; Signell and Geyer 1991). Wakes may

enhance mixing (Townsend et al. 1983) and modify sediment transport, thus influencing the bathymetry. Wakes can also have biological consequences that affect species-diversity gradients and plankton patchiness (Hamner and Hauri 1977, 1981), as well as the dispersal and settlement of reef fishes (Kingsford et al. 1991; Kingsford and Suthers 1996). For example, zooplankton can be entrained within convergence zones (Kingsford et al. 1991) or become concentrated within the reduced turbulence zones of gyrelike features (Aldredge and Hamner 1980; Murdoch et al. 1990). Aldredge and Hamner (1980) reported a 40-fold increase in zooplankton biomass within an eddy associated with a promontory near the Whitsunday Islands. Similar observations have been reported by Murdoch et al. (1990) off the west coast of New Zealand.

Hydrodynamically induced zooplankton patchiness is relevant to the establishment of the so-called recruitment hotspots of fish and invertebrates (Sammarco and Andrews 1988, 1989; Kingsford et al. 1991; McNiell et al. 1992). These regions could be identified from variations in the physical processes and patterns of water turbidity of island

## *Acknowledgments*

We are grateful to the crew and captain of the RV *Franklin*, along with the Commonwealth Scientific and Industrial Research Organisation personnel who contributed to the success of the cruise. We acknowledge constructive discussions with C. Reiss and K. Thompson at Dalhousie University and two anonymous reviewers. Geo-Science Australia, the National Tidal Facility at Flinders University and B. Petrie assisted with bathymetry data and tidal interpretation. We thank R. Piola and S. Murray for the zooplankton analyses.

Funding was provided by the Australian Research Council; the Department of Industry, Trade and Commerce; the Australian Geographic magazine; Focal Technologies; the Canada Department of Fisheries and Oceans; and the Natural Sciences and Engineering Research Council of Canada.

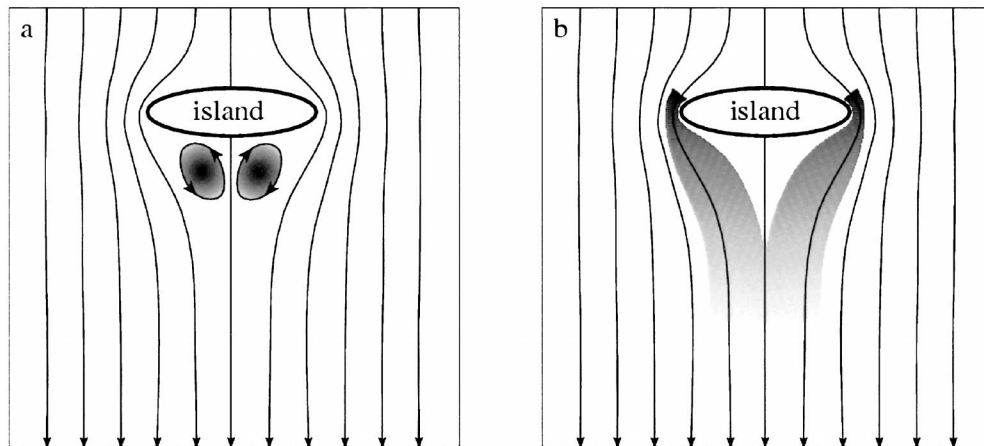


Fig. 1. Illustration of two processes generating near-surface patterns of sediment-laden plumes in shallow island wakes. (a) EU within paired lee eddies brings sediment-laden waters to the surface, and (b) EA is where swift currents at the island edge erode and suspend sediments and create plumes that advect long streamlines until particles sink back to deep water. The two processes may be complementary.

wakes. We could therefore explain spatial and temporal variation in the biological assemblages of plankton and larvae as they approach settlement.

In the present study, two physical processes that could produce a near-surface expression of bottom-preferential tracers (sedimentary and biological) are examined. The first is the eddy upwelling (EU) that arises from the vertical suction of fluid from the benthic boundary layer below rotating flows (Greenspan 1968; Wolanski et al. 1984a; Pattiaratchi et al. 1986). This process may draw near-bottom sediments and biota toward the centers of eddies and thence to the water surface, yielding a surface signature of isolated patches centered on eddies in the lee of islands (Fig. 1a). The second process involves seabed erosion and the entrainment of sediments upward into the water column, preferentially in the high-velocity region near the flanks of the island. The advection of this entrained fluid within the converging streamlines may yield a V- or Y-shaped surface signature in the island lee (Fig. 1b). We denote erosion, vertical mixing, entrainment, and advection as “EA.” This process was probably first identified by Leonardo da Vinci (Levi 1995) in observations and sketches around stones in shallow streams. The process is well known in aerodynamic and coastal engineering literature and is described as horseshoe vortices (Thwaites 1960). The relative importance of the EU and EA processes, as illustrated in Fig. 1, can be distinguished from field observations.

We report here on the spatial variation in flow field, light attenuation (a proxy for turbidity and suspended sediment), and zooplankton size and abundance estimates derived from an acoustic Doppler current profiler (ADCP) and an optical plankton counter (OPC) in the flood tide wake of a small (2 km) island in the shallow coastal region of the Great Barrier Reef. The majority of the measurements were obtained throughout the water column with the ship under way, at nominal speeds of 1–2 m s<sup>-1</sup>, in an effort to secure a reasonably synoptic view of the semidiurnally varying system. These measurements were supplemented with neuston net

collections across the wake, to provide a series of point estimates of the zooplankton and larval fish assemblages.

## Materials and methods

*Study area and data collection*—Derwent Island (21°00'S, 149°49'E) is a low-relief island in the Northumberland Island group of the Great Barrier Reef and is located south of the Whitsunday Islands and 70 km east of the town of Mackay, Queensland, Australia (Fig. 2). The island's long axis is ~2 km east-west and normal (80°) to the strong tidal flows that are focused on Broad Sound to the south, where the tidal range may exceed 10 m (Middleton et al. 1984). The clockwise semidiurnal tidal excursion ellipse for the Derwent Island region has a main axis that is 9 km long (Middleton et al. 1984). The island has no fringing reef, and it presents an abrupt obstacle to the ebb (northward flowing) and flood (southward flowing) tidal currents that predominate. A small rocky reef is located 1 km northwest of Derwent, and Skull Rock (which is exposed at low tide) is located 0.5 km east of the island. The only other reef within the tidal ellipse is Three Rocks (149.74°E, 20.95°S), which is located 5 km northwest of Derwent. Otherwise, the surrounding bathymetry is featureless, the average depth within a 5-km radius of the Island being 45 m (SD = 5).

*Current measurements*—Data were collected south of Derwent Island aboard the RV *Franklin* (cruise FR 02/93) at night during the flood tide. The ship steamed at nominal speeds of 1–2 m s<sup>-1</sup> across five transects (T<sub>1</sub>–T<sub>5</sub>; 5–8 km long) through the flood tide wake, beginning the night of 11 February 1993, and across four transects (T<sub>2</sub>1–T<sub>2</sub>4; each 5.5 km long), beginning the night of 12 February 1993. Transects were located between 1 and 5 km south of the island, and each took ~1 h to complete (Fig. 3, Table 1). On each transect, we recorded global positioning system navigational data and depth-varying currents, the latter from a hull-mounted 300-KHz RDI Instruments ADCP, averaging over

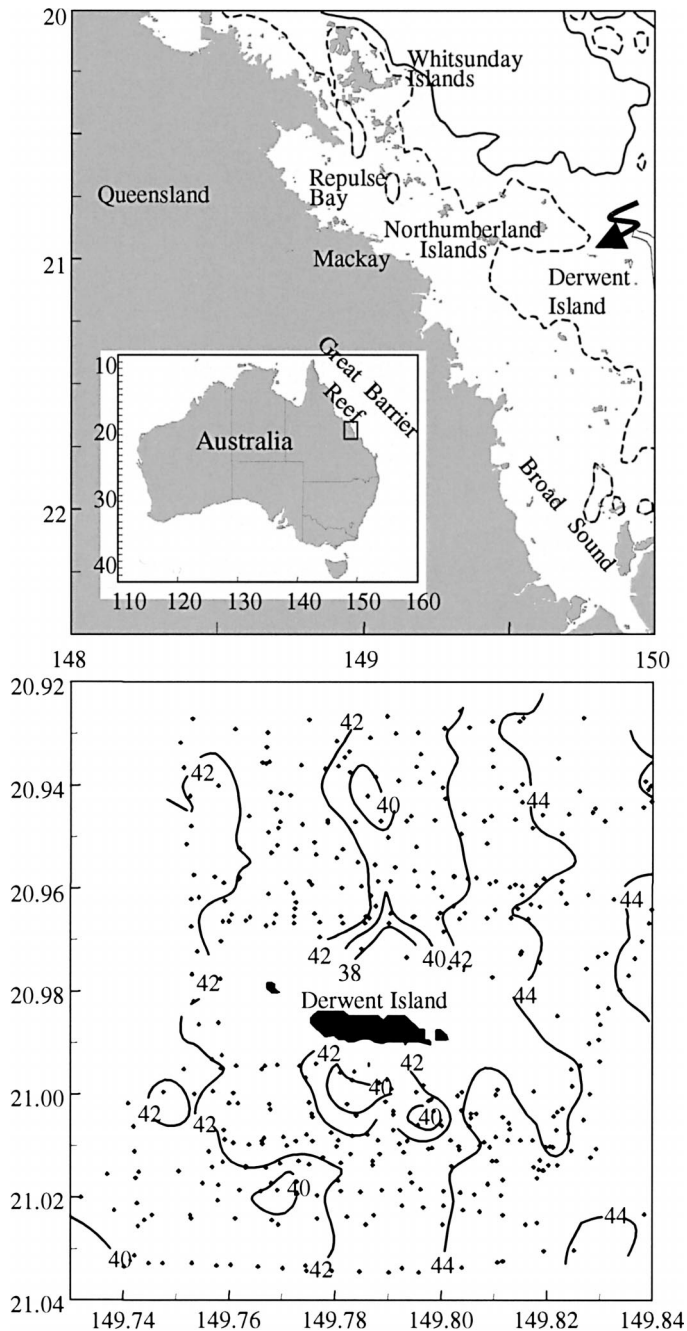


Fig. 2. Bathymetric (25- and 50-m isobaths) chart of the east coast of Queensland, Australia, and the Great Barrier Reef (inset), showing the location of Derwent Island within the Northumberland Island group (upper panel) and the local bathymetry (2-m isobath intervals; no correction for tide) surrounding Derwent Island as determined using depth estimates (black dots) provided from the vessel depth sounder (lower panel).

4-m depth strata beginning 12.4 m below the surface. Data were subsequently time-averaged into 3-min intervals to yield  $\sim 250$ -m profile spacing.

*Optical plankton count measurements*—On all transects except  $T_{24}$ , physical and biological properties of the water

column were measured using the Towed Underwater Biological Sensor System (TUBSS; Sprules et al. 1992; Taggart et al. 1996; Rissik et al. 1997). Designed and built at Dalhousie University, the system consisted of an Endeco V-fin fitted with a Focal Technologies OPC (Herman 1988), an Ocean Sensors OS-100 conductivity, temperature, and depth (CTD) sensor fitted with pitch and roll sensor (for use in monitoring V-fin attitude and for correcting OPC sample volumes), and a General Oceanics digital flowmeter (for estimating the OPC sample volume). With the exception of the OPC, which transmitted data in real time, all other TUBSS data were transmitted via an integrated data stream from the CTD through the conducting tow cable to the ship for computerized logging at 0.5 Hz.

The OPC measures (mV) light attenuation in the water column, which is used as an index of water color and turbidity from phytoplankton and suspended sediments  $<250$ - $\mu\text{m}$  equivalent spherical diameter (ESD). The OPC also counts and sizes any optically refractive particles nominally  $>250$ - $\mu\text{m}$  ESD, and data are recorded among 4,096 calibrated digital sizes that are proportional to the projected particle area. We reclassified the particle data into 64 size classes, which are expressed as a geometric mean ESD ( $\mu\text{m}$ ) on the basis of the integer value of the square root of 4,096 digital size classes (Table 2 and as in Taggart et al. 1996). The volume of water sampled and the particle counts within each of the 64 size classes were summed over sequential 2-s intervals, to provide data at a rate of 0.5 Hz to match that of the other instruments. OPC data logging required file breaks (data interruption period normally  $<60$  s) at 30-min intervals. For practical purposes, only 13 of the 64 size classes were analyzed and include the smallest reliably resolved size class (318- $\mu\text{m}$  ESD) to the largest reasonably abundant size class (1,893  $\mu\text{m}$ ; Table 2). OPC number-at-size estimate data can be distorted by particle coincidence (when two or more particles simultaneously interrupt the light beam at high particle concentrations). According to Sprules et al. (1992), coincidence may distort 10% of the data at concentrations of 11 particles  $\text{L}^{-1}$ . Because our data provided an overall average concentration of  $<6$  particles  $\text{L}^{-1}$  and a maximum of 10 particles  $\text{L}^{-1}$ , we inferred that coincidence affected  $<10\%$  of our data.

On the night of 11 February, five transects (Fig. 3a) were completed during the flood tide period. On  $T_{11}$  and  $T_{12}$ , the instrument was towed at 11-m depth, and on  $T_{15}$  at 17-m depth, to maximize the horizontal resolution (3 m) in the surface layer. On  $T_{13}$  and  $T_{14}$ , the instrument was undulated over depths of 4–30 m, to attain improved vertical resolution (1 m) at a cost to horizontal resolution (140 m).

On the night of 12 February, three 5.5-km transects (Fig. 3c) were completed within the flood tide period by undulating the TUBSS between 4- and 30-m depth across the wake, providing similar spatial resolution as obtained by the method described above. We subsequently completed an extra transect,  $T_{25}$ , on the north side of the island along latitude 20.96°S between 149.860°E and 149.795°E during the early morning of 13 February (Table 1). The eastern half of  $T_{25}$  was completed during the remainder of the flood tide (southward flowing) and permitted a brief examination of the upstream flow prior to its being disturbed by the island.

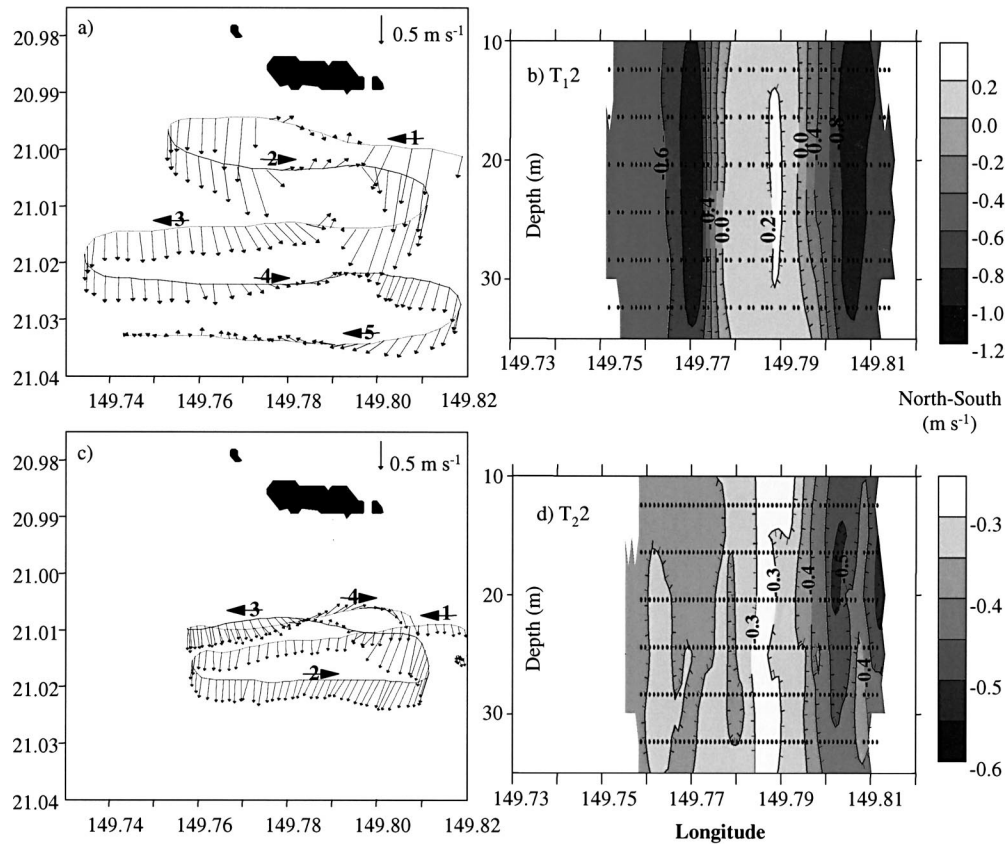


Fig. 3. ADCP depth-averaged surface layer (12.4 m) current vectors along transects south of Derwent Island during flood tide on the nights of (a) 11 February and (c) 12 February and corresponding longitudinal section profiles of velocity ( $u$ -components; positive north) and scale bars ( $\text{m s}^{-1}$ ) along (b)  $T_{1,2}$  and (d)  $T_{2,2}$  as estimated over six 4-m depth strata (12.4–32.4 m). Integers superimposed over an arrow (steaming direction) in panels a and c denote sequential transect numbers for each night.

Table 1. Summary of transect data collected across the flood-tide wake on the south side of Derwent Island, showing the date in February 1993. Listed is the transect number (east or west heading), local time (total minutes on transect), depth range of the TUBSS, number of records, number of undulations (“tow-yos”), the figure number of the corresponding vertical section, neuston net sample station identifiers as shown in Fig. 12, range in concentration of total larval fish (per  $250 \text{ m}^3$ ), and corresponding range in Shannon-Weiner diversity indices. High tide at Mackay was at 0235 and 1454 h on February 12 (5.0 and 4.5 m, respectively).

Date and transect	Local time (min.)	TUBSS (m)	No. of records	No. of tow-yos	Figure	Neuston samples	Total larvae	Shannon
11–12 Feb								
$T_{1,1}$ ( $\leftarrow$ )	2129–2210 (41)	11	1,199	—	—	—	—	—
$T_{1,2}$ ( $\rightarrow$ )	2213–2255 (42)	11	1,223	—	—	—	—	—
$T_{1,3}$ ( $\leftarrow$ )	2301–2356 (55)	4–27	1,619	21	8*	—	—	—
$T_{1,4}$ ( $\rightarrow$ )	0003–0115 (72)	4–30	2,091	30	9	—	—	—
$T_{1,5}$ ( $\leftarrow$ )	0121–0217 (56)	17	1,638	—	—	—	—	—
12–13 Feb								
$T_{2,1}$ ( $\leftarrow$ )	2128–2224 (56)	4–30	1,657	22	10a	$T_{2,1a-h}$ ( $n = 8$ )	181–402	0.9–1.2
$T_{2,2}$ ( $\rightarrow$ )	2236–2343 (67)	4–30	1,994	31	10b	$T_{2,2a-h}$ ( $n = 8$ )	259–555	0.8–1.3
$T_{2,3}$ ( $\leftarrow$ )	0002–0049 (47)	4–30	1,403	19	10c	$T_{2,3a-f}$ ( $n = 6$ )	248–603	1.0–1.5
$T_{2,4}$ ( $\rightarrow$ )	(ADCP only)	—	—	—	—	—	—	—
13 Feb								
$T_{2,5}^\dagger$ ( $\leftarrow$ )	0252–0317 (25)	4–30	752	9	11	—	—	—

\* The horizontal distribution of all five transects is shown in Fig. 7.

† Transect on the north side of Derwent Island during the final stages of flood tide.

Table 2. List of OPC digital size classes (bins), the geometric mean equivalent spherical diameter (ESD), and the biomass of a particle in each class, under the assumption of a density of  $1,000 \text{ kg m}^{-3}$ . The average unrotated loadings (factors) of a PCA (% variance explained) of the biomass in size classes are shown. These groupings defined the small- and medium-size zooplankton particles. The taxonomic composition of particles  $>5\%$  of those examined and the range of their size categories is indicated, with their average size category indicated in boldface type (determined from image analysis of their maximum lateral area). Detritus occurred in all size categories.

Digital size category	ESD ( $\mu\text{m}$ )	Biomass (mg)	Factor 1 (35%)	Factor 2 (14%)	Composition
9–15	318	0.0168	0.92	–0.13	
16–24	425	0.0402	0.92	–0.04	<i>Undinula</i>
25–35	535	0.0802	0.90	0.16	<i>Undinula</i> , <i>Centropages</i>
36–48	648	0.1425	0.60	0.65	<i>Undinula</i> , <i>Eucalanus</i> , zoea, <i>Centropages</i> , carid
49–63	764	0.2335	–0.25	0.86	<b><i>Undinula</i></b> , <i>Eucalanus</i> , zoea, <i>Centropages</i> , carid
64–80	883	0.3605	–0.61	0.62	<i>Undinula</i> , <b><i>Eucalanus</i></b> , zoea, <b><i>Centropages</i></b> , carid
81–99	1,003	0.5283	–0.66	0.29	<i>Undinula</i> , <i>Eucalanus</i> , <b>zoea</b> , <i>Centropages</i> , carid
100–120	1,125	0.7455	–0.54	–0.03	<i>Eucalanus</i> , zoea, <i>Centropages</i> , carid
121–143	1,249	1.0202	–0.44	–0.08	<i>Eucalanus</i> , zoea, carid
144–168	1,375	1.3612	–0.44	–0.20	<i>Eucalanus</i> , <i>Sagitta</i> , zoea, carid
169–195	1,502	1.7742	–0.40	–0.18	<i>Eucalanus</i> , <i>Sagitta</i> , zoea, <b>carid</b>
196–224	1,631	2.2717	–0.29	–0.21	<i>Eucalanus</i> , <i>Sagitta</i> , zoea, carid
225–255	1,761	2.8594	–0.38	–0.21	<i>Sagitta</i> , carid
256–288	1,893	3.5518	–0.26	–0.21	<i>Sagitta</i> , carid

*Neuston collections*—Surface zooplankton were collected on transects T<sub>2</sub>1–T<sub>2</sub>3 on the night of 12 February (coincident with ADCP and TUBSS) using a 0.75-m-square 330- $\mu\text{m}$  mesh net deployed 2–3 m outboard from the vessel. A General Oceanics flowmeter was used to determine the total filtered volume (nominally  $250 \text{ m}^3$  per collection). The net was sequentially deployed for 5-min periods in a spatial series fashion on each transect. Each deployment was followed by a 2-min interval to retrieve, clean, and redeploy the net. This protocol provided 22 collections over the three transects and a horizontal resolution of 600 m (Table 1). Net collections were preserved immediately in 5% (vol/vol) buffered formaldehyde and seawater. Because samples were collected at night, we assume that species- and size-specific avoidance were minimized. Samples were subsequently sorted, and fish larvae were identified by taxonomic family (Leis and Rennis 1983; Leis and Trnski 1989), enumerated, and analyzed as a concentration (individuals per  $250 \text{ m}^3$ ) or individuals  $\text{m}^{-3}$ .

The 13 calibrated OPC size classes were taxonomically referenced using individuals of the different taxa in the net collections. First, we determined the range of sizes for the different taxa among concentrated subsamples taken from seven different net collections representative of the three transects. Each subsample was mixed, placed in a linear trough (5 ml), and examined using a video camera mounted on a microscope. The trough was scanned in one direction, and the first 100 particles in each sample, including detritus, were identified, outlined (including copepod antennae and excluding setae) using NIH-Image software (available at <http://rsb.info.nih.gov/nih-image/>), and the calculated area was converted to equivalent spherical diameter (Rissik et al. 1997).

To compare OPC estimates of abundance among size classes with net collection estimates, we used image analysis and quantitative subsamples drawn from the same seven concentrated collections for image analysis. Each was diluted to 250 ml, mixed, and three replicates of 1-ml subsamples

were withdrawn. Each was placed under the camera, and seven fields of view (with no overlap) were selected haphazardly to create image “stack.” Particles (10–60 per field) were then sized (using image area converted to  $\mu\text{m}$  ESD as for the OPC), classified according to the 13 OPC size classes, and summed by size class and expressed as a concentration (particles  $\text{m}^{-3}$ ). Size and abundance estimates of the neustonic zooplankton provided by image analysis were within 25% of the OPC’s near-surface estimates for the small- and medium-sized particles ( $<764 \mu\text{m}$  ESD). The OPC’s abundance estimates of larger particles declined from 43% of the image analysis estimate of neuston (883  $\mu\text{m}$ ) to 11% (1,502  $\mu\text{m}$ ). This systematic divergence in abundance-at-size is a function of size-related avoidance of the OPC opening, which is small relative to the neuston net opening (Hopcroft 2002), the large volume sampled by the neuston net relative to the OPC (170:1) and the consequent under-sampling by the OPC of large particles at low concentration (e.g., Huntley et al. 1995), and that the OPC collected data 4–10 m below that sampled by the neuston net. Our image analysis method may also be biased, because larger zooplankton have an increased likelihood, relative to the OPC, of presenting the maximum sectional area to the camera.

*Analyses*—OPC particle abundance-at-size data were converted to concentration (number  $\text{m}^{-3}$ ) and along with the temperature, light attenuation, and depth data were smoothed using a symmetrical, cosine-weighted (–0.041, –0.01, 0.119, 0.267, and 0.33), nine-point moving average (Legendre and Legendre 1998). The smoothing algorithm resulted in some small negative estimates when blocks of data containing zero estimates (for the relatively rare large particles  $>1,000\text{-}\mu\text{m}$  ESD) were encountered. These were set to zero. The biomass of each size class (expressed in mg; Table 2) was estimated using the concentration-at-size estimates under the assumption that individual spherical particles have a near-neutral density of  $1,000 \text{ kg m}^{-3}$ .

A principal-components analysis (PCA; no rotation of axes) of the log-transformed [ $\ln(x + 1)$ ] zooplankton biomass concentrations ( $x$ ) in each of the 13 size classes was done on the data from  $T_{13}$  and  $T_{21}$ , and the results were used to reclassify the 13 size classes into either a small size class (318–535- $\mu\text{m}$  ESD) or a medium size class (764–1,003- $\mu\text{m}$  ESD) (Table 2). The neustonic larval fish data were also subject to a PCA (transformed as above), using varimax rotation of axes to generate unconfounded factor scores (providing interpretive insights by redistributing factor loadings among taxa such that each taxon tends to be associated with one factor). We used only the 11 most abundant taxonomic families, which were present in at least half ( $\geq 11$  of 22) of the net collections.

Contours of surface and sectional variation of the flow field, light attenuation, and zooplankton biomass were generated (Surfer; Golden Software) using a kriging algorithm with a conservative gridding routine with dimensions determined by the average  $x$  and  $y$  spacing of the data. For example, when contouring the vertical section data, we used a  $50 \times 33$ -node grid derived from the number of vertical profiles ( $x$ ) and 1-m depth intervals ( $y$ ), a quadrant search radius with anisotropy set at 10% of the  $x$ ,  $y$  range, a maximum of 24 data per node within the search radius, and blanking where  $< 12$  data were within the search radius. The resultant grid was then matrix smoothed using a twofold weight on the center node to produce a new grid with twice (interpolated) the resolution of the original. When contouring the surface layer data from the five transects beginning on 11 February, we used all of the constant depth data from transects  $T_{11}$  and  $T_{12}$  (11 m) and  $T_{15}$  (17 m) and the 9–15-m-depth-averaged data on transects  $T_{13}$  and  $T_{14}$ , when the TUBSS undulated through the water column to gather sectional data (Table 1).

## Results

**Derwent Island wake**—The flow field from the ADCP data during the flood tide of 11 February shows a wake due south of the island (transects  $T_{11}$ – $T_{15}$ ; Figs. 3a, 4). The currents were  $< 0.5 \text{ m s}^{-1}$  throughout the water column in the lee of the island and were frequently directed to the east (Fig. 4e–h). Free-stream currents at the western extremities of the first four transects show a relatively constant free-stream southward flow of  $0.5 \text{ m s}^{-1}$  that was generally independent of depth (Figs. 3b, 4). Immediately downstream of the flanks of the island on transects  $T_{11}$  and  $T_{12}$ , the flow was  $> 1.0 \text{ m s}^{-1}$  throughout the water column (Fig. 4). The flow field on the second night (12 February) was analogous to that on the first, with similar patterns in the surface horizontal expression and in the vertical sections (Figs. 3c,d, 5), although current speeds were 30% weaker.

**Horizontal distribution of light attenuation and zooplankton**—On 11 February, we observed high (2,000–2,300 mV) local maxima in light attenuation at 9–14 m depth west of the Derwent wake on  $T_{11}$  and  $T_{12}$  and smaller (2,000 mV) local maxima to the east (Fig. 6). These regions correspond to regions of the highest current velocity (Fig. 7a). Light attenuation was lowest ( $< 2,000 \text{ mV}$ ) within the wake im-

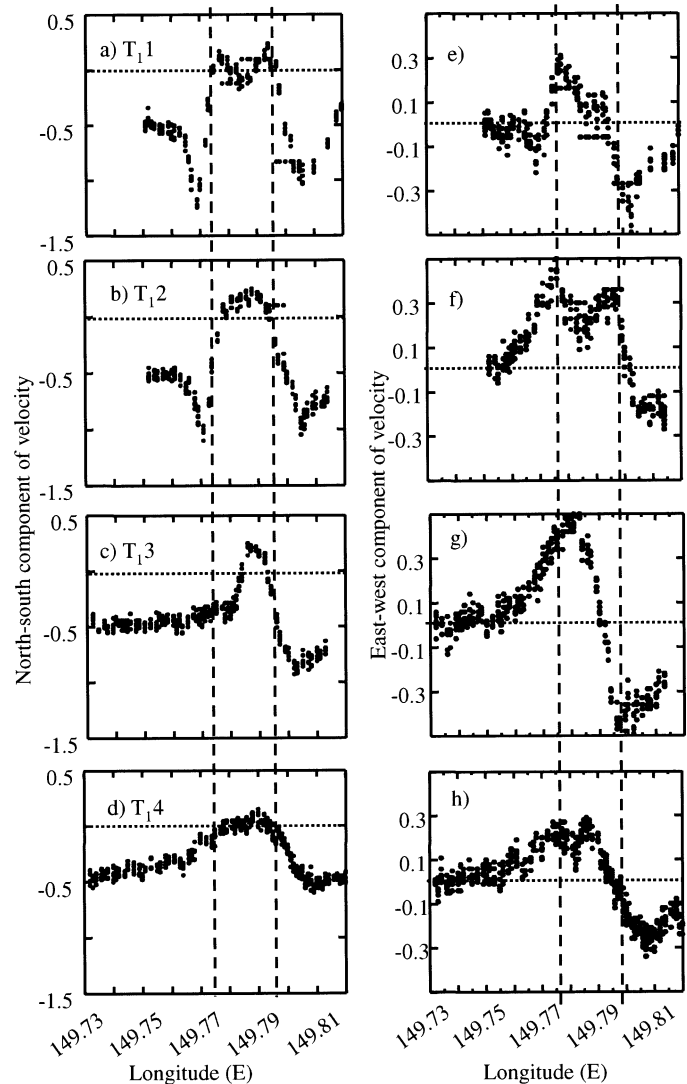


Fig. 4. Longitudinal section scattergrams a–d of  $u$  (positive N) and e–f of  $v$  (positive E) among six depth strata (12.4–32.4 m) along four transects south of Derwent Island during the flood-tide period beginning the night of 11 February. Each datum represents a current velocity estimate ( $\text{m s}^{-1}$ ) within one of the six depth strata as the ship steamed along each transect that increased in distance from the island, as illustrated in Fig. 3. The dashed vertical lines represent the eastern and western edges of Derwent Island located upstream; the dotted horizontal reference line is at  $0 \text{ m s}^{-1}$ .

mediately south of the island ( $T_{11}$  and  $T_{12}$ ; Figs. 6a,b, 7a) as well as in the free stream well to the east and west of the wake region ( $T_{13}$ – $T_{15}$ ; Fig. 7a). There was some evidence that the local maxima on  $T_{11}$  and  $T_{12}$  to the west of the wake region (and less so to the east on  $T_{12}$ ) were contiguous with the decreased central maxima on  $T_{13}$  and  $T_{14}$  that became further dissipated during the slackening tide by the time  $T_{15}$  was completed. The general pattern of distribution of light attenuation in the near-surface layer was consistent with that expected for a V- or Y-shaped plume downstream of the island.

The horizontal distribution of small zooplankton biomass was inversely related to the horizontal distribution of light

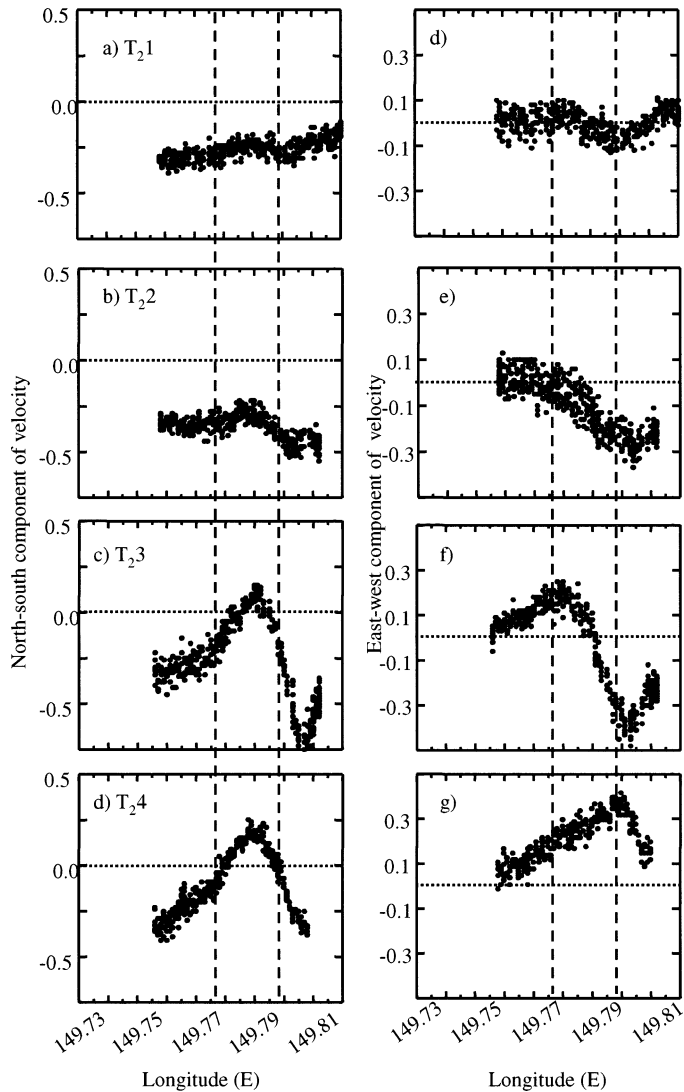


Fig. 5. Longitudinal section scattergrams a–d of  $u$  (positive N) and e–f of  $v$  (positive E) among six depth strata (12.4–32.4 m) along four transects south of Derwent Island during the flood-tide period beginning the night of 12 February. Each datum represents a current velocity estimate ( $\text{m s}^{-1}$ ) within one of the six depth strata as the ship steamed along each transect, as illustrated in Fig. 3. The dashed vertical lines represent the eastern and western edges of Derwent Island located upstream; the dotted horizontal reference line is at  $0 \text{ m s}^{-1}$ .

attenuance (Table 3,  $R = -0.71$ ,  $P < 0.001$ ; Fig. 7b), with concentrations generally  $< 100 \text{ mg m}^{-3}$  in those regions where attenuation was  $> 2,000 \text{ mV}$ . In contrast, the biomass of medium-sized zooplankton was positively associated with light attenuation, and the former tended to increase from north to south and reached a maximum of  $600 \text{ mg m}^{-3}$  by T<sub>1</sub>4 (Fig. 7c). This local maximum biomass persisted on T<sub>1</sub>5, although it was somewhat diminished ( $400 \text{ mg m}^{-3}$ ).

*Vertical distribution of light attenuation and zooplankton*—Temperature varied minimally over all depths and transects, ranging 27.2–27.6°C. The 5–25-m vertical profiles from T<sub>1</sub>3 on 11 February revealed two columns of greater

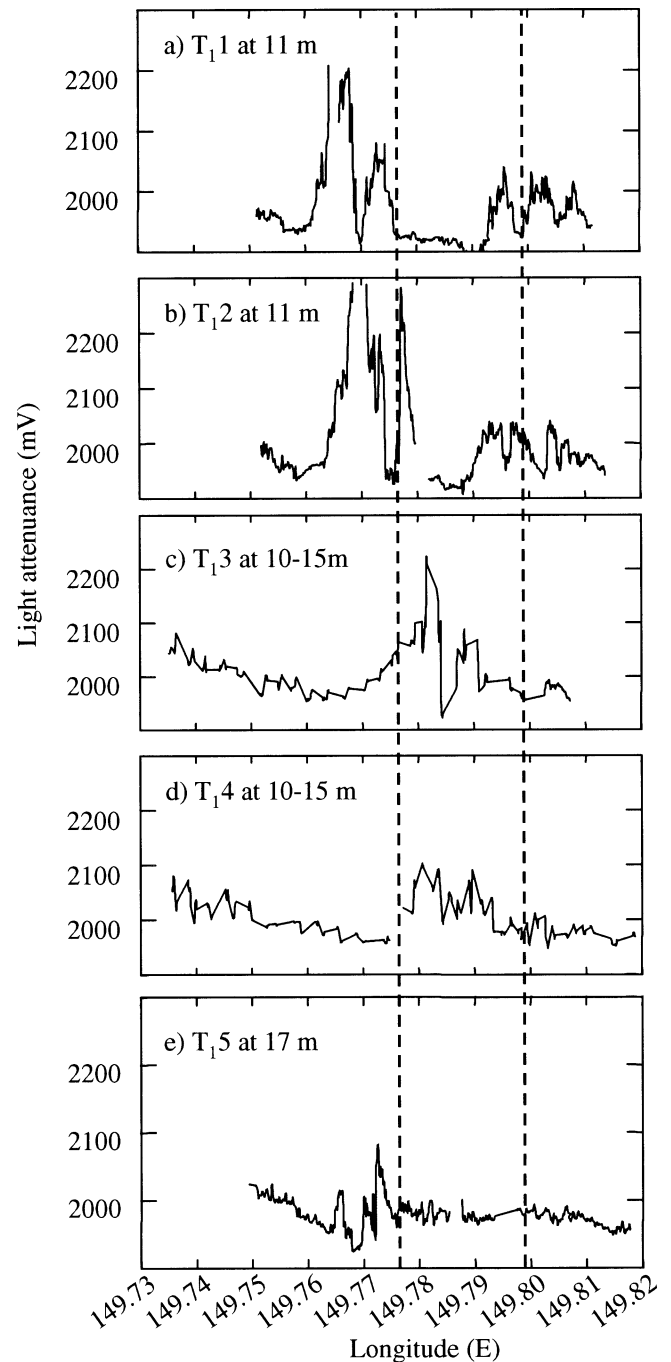


Fig. 6. Longitudinal section scattergrams of light attenuation (at 11-, 10–15-, or 17-m depth) along five transects south of Derwent Island during the flood-tide period beginning the night of 11 February as the ship steamed along each transect (a–e) that increased in distance from the island (see Fig. 3). The dashed vertical lines represent the eastern and western edges of Derwent Island, located upstream.

light attenuation downstream of the western and eastern promontories of the island (Fig. 8a; the corresponding horizontal expression for the 9–15 m depth range is shown in Fig. 7), although the western column was more pronounced (Figs. 6a,b, 8a). Further downstream, on T<sub>1</sub>4, only one col-

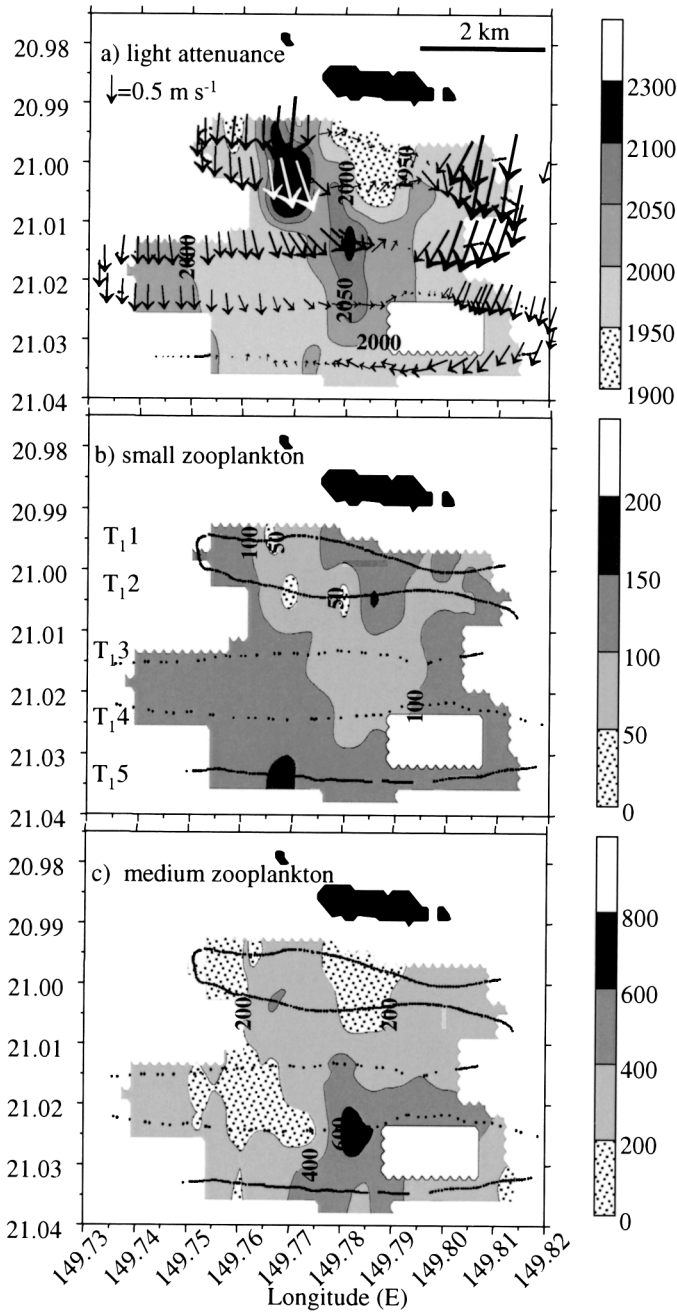


Fig. 7. Chart showing the horizontal distribution of (a) light attenuation (mV), (b) small (318–535- $\mu\text{m}$  ESD) zooplankton biomass concentration ( $\text{mg m}^{-3}$ ), and (c) medium-sized (764–1,003- $\mu\text{m}$  ESD) zooplankton biomass concentration (each with corresponding scale bar) in the island wake south of Derwent Island during the flood-tide period beginning the night of 11 February, as estimated using the OPC along the five transects (see Fig. 3). Current velocity vectors (as in Fig. 3) are overlain in panel a for reference, and the location of every tenth OPC datum along transects is shown in panels b and c. There are fewer estimates on T<sub>1,3</sub> and T<sub>1,4</sub> because the instrument was undulated throughout the water column and only the data in the 9–15-m depth stratum are used.

Table 3. Pearson correlation coefficients among temperature (Temp.), light attenuation (Atten.), biomass concentration of small- and medium-size zooplankton from two representative transects. Transect T<sub>1,3</sub> on 11 February ( $n = 1,614$ ) was below the diagonal, and T<sub>2,1</sub> on 12 February ( $n = 1,645$ ) was above the diagonal. Coefficients  $>0.06$  are significant.

	Temp.	Atten.	Small	Medium
Temp.	—	-0.30	0.50	-0.39
Atten.	-0.15	—	-0.69	0.45
Small	0.21	-0.71	—	-0.29
Medium	-0.23	0.53	-0.43	—

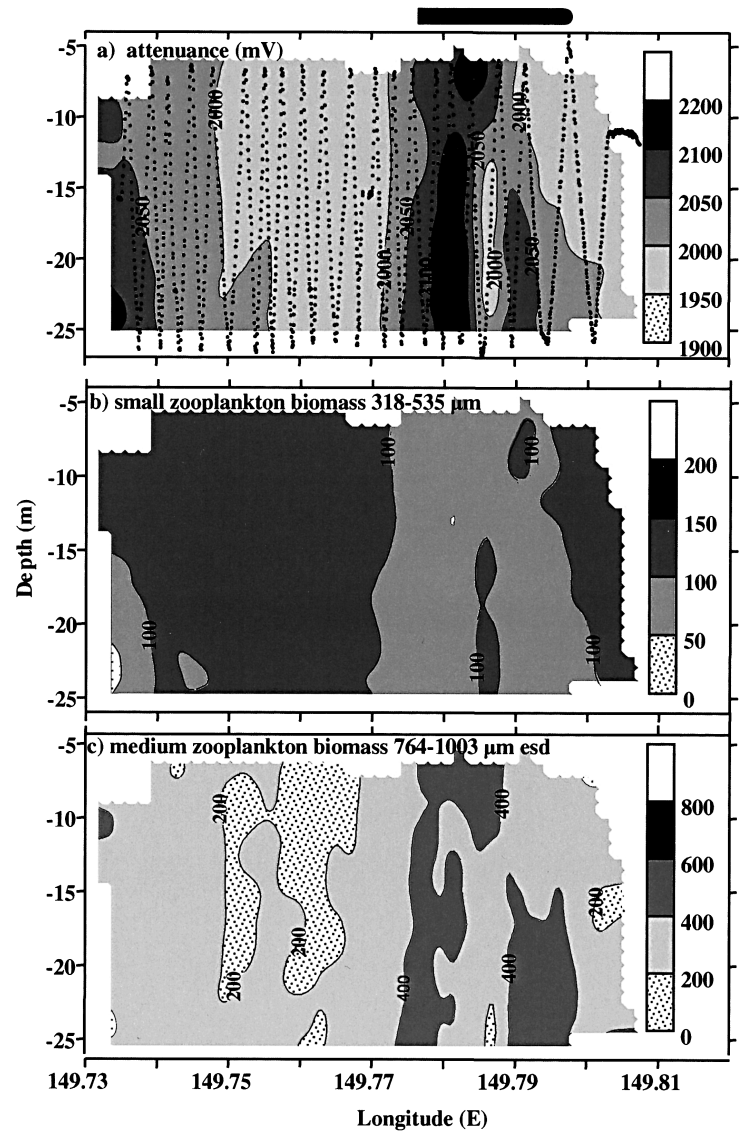


Fig. 8. Longitudinal section profiles of (a) light attenuation (mV), (b) small (318–535- $\mu\text{m}$  ESD) zooplankton biomass concentration ( $\text{mg m}^{-3}$ ), and (c) medium-sized (764–1,003- $\mu\text{m}$  ESD) zooplankton biomass concentration (each with scale bar) on transect T<sub>1,3</sub> during the flood-tide period starting the night of 11 February, where the location of each estimate (datum) from the OPC undulation is provided in panel a. The solid bar at the top of the figure represents the location of Derwent Island, upstream of the transect.

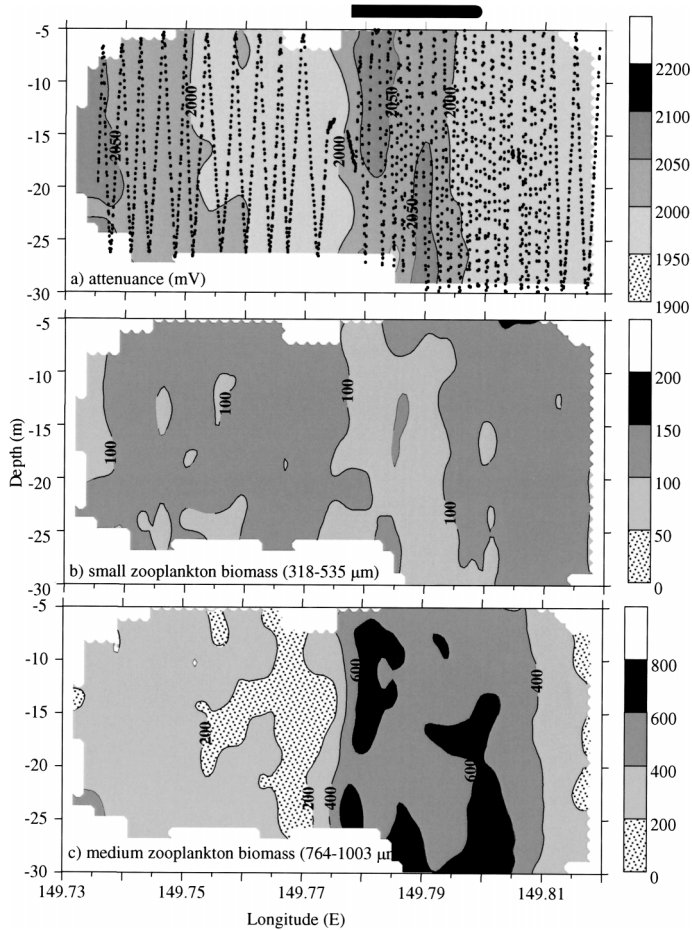


Fig. 9. Longitudinal section profiles of (a) light attenuation (mV), (b) small (318–535- $\mu\text{m}$  ESD) zooplankton biomass concentration ( $\text{mg m}^{-3}$ ), and (c) medium-sized (764–1,003- $\mu\text{m}$  ESD) zooplankton biomass concentration (each with scale bar) on transect  $T_{14}$  during the flood-tide period starting the night of 11 February, where the location of each estimate (datum) for the OPC undulation is provided in panel a. The solid bar at the top of the figure represents the location of Derwent Island, upstream of the transect.

umn of attenuation was apparent (Fig. 9a), which is consistent with the surface expression described above. Associated with the greater light attenuation signal, was a decrease in the biomass of small zooplankton that was  $>100 \text{ mg m}^{-3}$  outside the wake (Fig. 8b). In contrast, there was a marked increase in the biomass of medium-sized zooplankton immediately downstream of the island (Fig. 8c). As with the current, temperature, and light attenuation profiles, there was little evidence of vertical variation in zooplankton biomass. A similar pattern was observed on  $T_{14}$  (Fig. 9), where the biomass concentrations of medium-sized zooplankton ( $400 \text{ mg m}^{-3}$ ) persisted throughout the water column and were three- to fourfold greater than that observed in the free stream (Fig. 9c).

On 12 February,  $T_{21}$  also revealed relatively uniform columns of greater light attenuation throughout the water column (data not shown). These were located downstream of the island's eastern and western limits and, as before, approximated the location of increased medium-sized zoo-

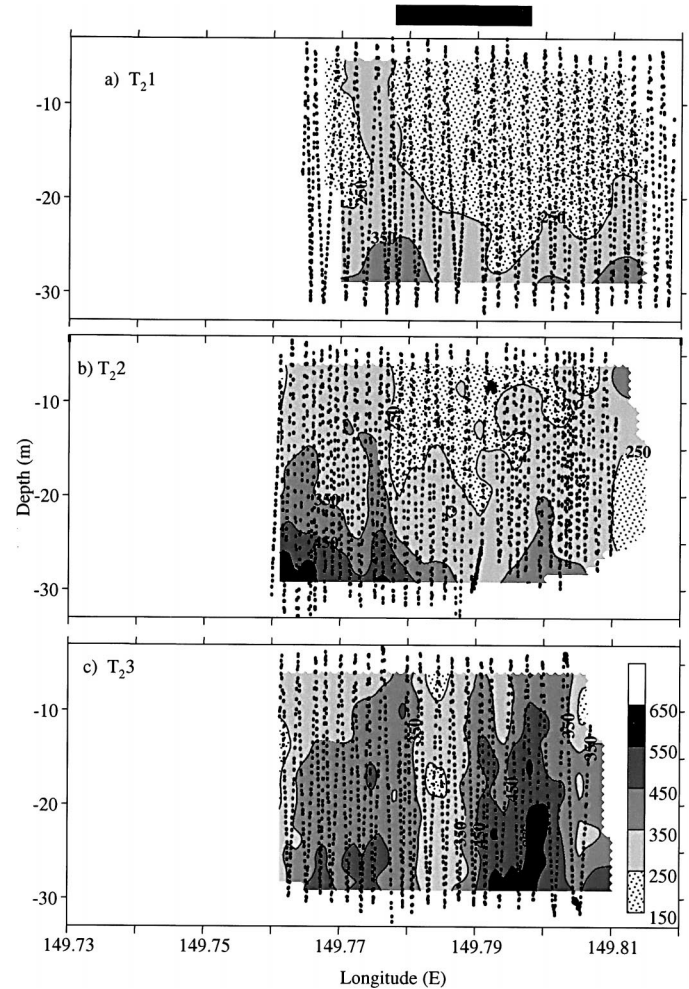


Fig. 10. Longitudinal section profiles of medium-sized (764–1,003- $\mu\text{m}$  ESD) zooplankton biomass concentration ( $\text{mg m}^{-3}$ ), with scale bars, along transects (a)  $T_{21}$ , (b)  $T_{22}$ , and (c)  $T_{23}$  south of Derwent Island during the flood-tide period beginning the night of 12 February, where the location of each estimate (datum) for the OPC undulation is provided. The solid bar at the top of the figure represents the location of Derwent Island, upstream of the transect.

plankton biomass—particularly at the western end (Fig. 10a). This pattern was enhanced on  $T_{22}$  and  $T_{23}$ , because the  $>250 \text{ mg m}^{-3}$  contour extended above 10-m depth (Fig. 10b,c). On all transects, the central wake region downstream of the island had the lowest measures of light attenuation and the lowest concentrations of medium-sized zooplankton biomass.

Upstream of Derwent Island during the final stages of the flood tide ( $T_{25}$ , current  $<0.2 \text{ m s}^{-1}$  southward), the water column showed some stratification in light attenuation (Fig. 11), with values ( $<1,900 \text{ mV}$ ) similar to those observed in the free stream on earlier transects. The small zooplankton biomass was more concentrated ( $>110 \text{ mg m}^{-3}$ ) in the near-surface layer, and the medium-sized zooplankton biomass was more concentrated in deeper water, at  $>20\text{-m}$  depth ( $300\text{--}500 \text{ mg m}^{-3}$ ; Fig. 11b). The biomass concentration of small zooplankton upstream was similar to that observed in low light attenuation waters downstream (Figs. 7b, 9b),

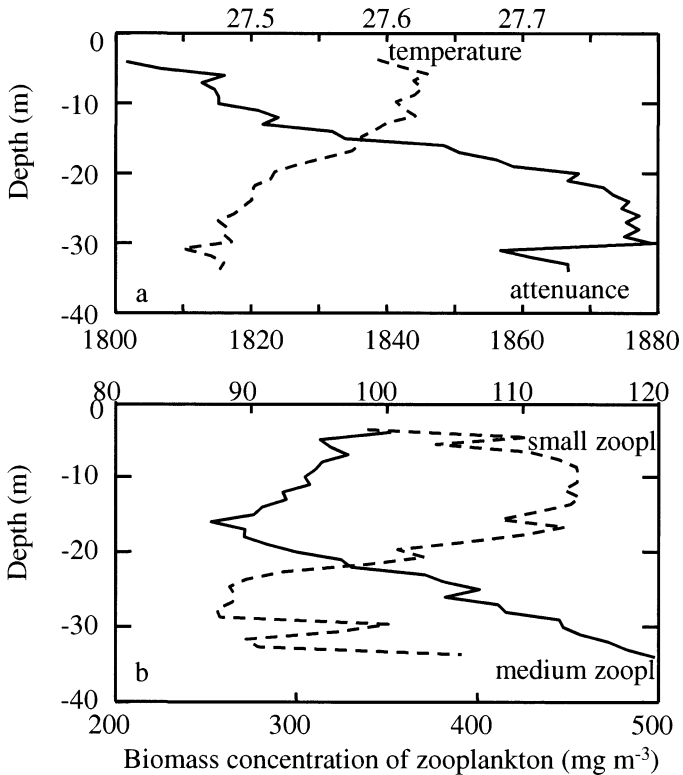


Fig. 11. Vertical profiles of (a) temperature (dashed line), light attenuation (solid line), and (b) small (318–535- $\mu\text{m}$  ESD, dashed line) and medium-sized (764–1,003- $\mu\text{m}$  ESD, solid line) zooplankton biomass concentration ( $\text{mg m}^{-3}$ ) averaged over 1-m depth strata from transect T<sub>2</sub>5 (Table 1) located on the northeast side of Derwent Island (i.e., upstream of the island), along 20.97°S, 149.81–149.78°E during the late flood tide.

whereas that of medium-sized zooplankton upstream was less than half that observed within the wake (Figs. 9c, 10).

**Surface ichthyoplankton**—The 22 neuston net collections along T<sub>2</sub>1, T<sub>2</sub>2, and T<sub>2</sub>3 on the night of 12 February produced 7,031 larvae representing 38 families (Table 4). The concentrations of total larval fish averaged 350 (SE = 25) per standardized haul, and the Shannon-Weiner diversity index averaged 1.09 (SE = 0.03) across the wake. The samples were dominated by 11 families that occurred in at least 11 of the 22 samples (Table 4). The PCA of these families produced two groupings, one composed of bregmacerotids, gobies, carangids, leiognathids, platycephalids, and priacanthids in factor 1, and the other composed of gerreids, bothids, and nemipterids in factor 2 (Table 5). Over all three transects, factor 1 was significantly correlated with the average biomass of medium-sized zooplankton ( $R = 0.43$ ,  $P < 0.001$ ; Fig. 12a) and average light attenuation ( $R = 0.48$ ,  $P < 0.001$ ) estimated using the OPC data collected coincidentally with each neuston net collection. Factor 2 was negatively correlated with medium-sized zooplankton ( $R = -0.47$ ,  $P < 0.001$ ; Fig. 12b) and attenuation ( $R = -0.33$ ,  $P < 0.001$ ).

The zooplankton composition in the neuston net was compared between T<sub>2</sub>1 (samples T<sub>2</sub>1a–d) and T<sub>2</sub>2, T<sub>2</sub>3 (samples

Table 4. Percentage composition ( $n = 7,031$ ) of the 38 taxonomic families of larval fish identified among the 22 5-min neuston net samples collected across the flood-tide wake of Derwent Island during the night of 12 February.

Family	%
Gobiidae	68.13
Bregmacerotidae	7.28
Apogonidae	3.11
Gerreidae	2.19
Carangidae	1.83
Leiognathidae	1.56
Priacanthidae	1.34
Nemipteridae	1.24
Platycephalidae	0.87
Synodontidae	0.64
Pseudochromidae	0.47
Bothidae	0.44
Plesiopidae	0.30
Clupeidae	0.28
Callionymidae	0.23
Labridae	0.21
Terapontidae	0.18
Scorpaenidae	0.17
Pomacentridae	0.16
Microdesmidae	0.16
Atherinidae	0.10
Exocetidae	0.10
Antennariidae	0.09
Dactylopteridae	0.09
Cynoglossidae	0.07
Sillaginidae	0.07
Blenniidae	0.06
Acanthuridae	0.04
Monacanthidae	0.04
Tetradontidae	0.03
Belonidae	0.03
Lutjanidae	0.03
Scombridae	0.03
Centriscidae	0.01
Trichiuridae	0.01
Notosudidae	0.01
Hemiramphidae	0.01
Pempheridae	0.01

Table 5. Rotated component loadings of a PCA of the number of larval fish in each of 11 families present in >11 of the 22 5-min neuston net samples when collected across the flood-tide wake of Derwent Island during the night of 12 February, when Factor 1 explained 29% of the total variance and Factor 2 explained 17%.

Family	Factor 1	Factor 2
Bregmacerotidae	0.87	0.01
Gobiidae	0.75	0.28
Carangidae	0.68	-0.19
Platycephalidae	0.64	-0.06
Leiognathidae	0.63	0.04
Gerreidae	0.12	0.88
Bothidae	-0.38	0.71
Nemipteridae	0.11	0.61
Priacanthidae	0.49	0.36
Synodontidae	-0.23	-0.12
Apogonidae	0.32	-0.01

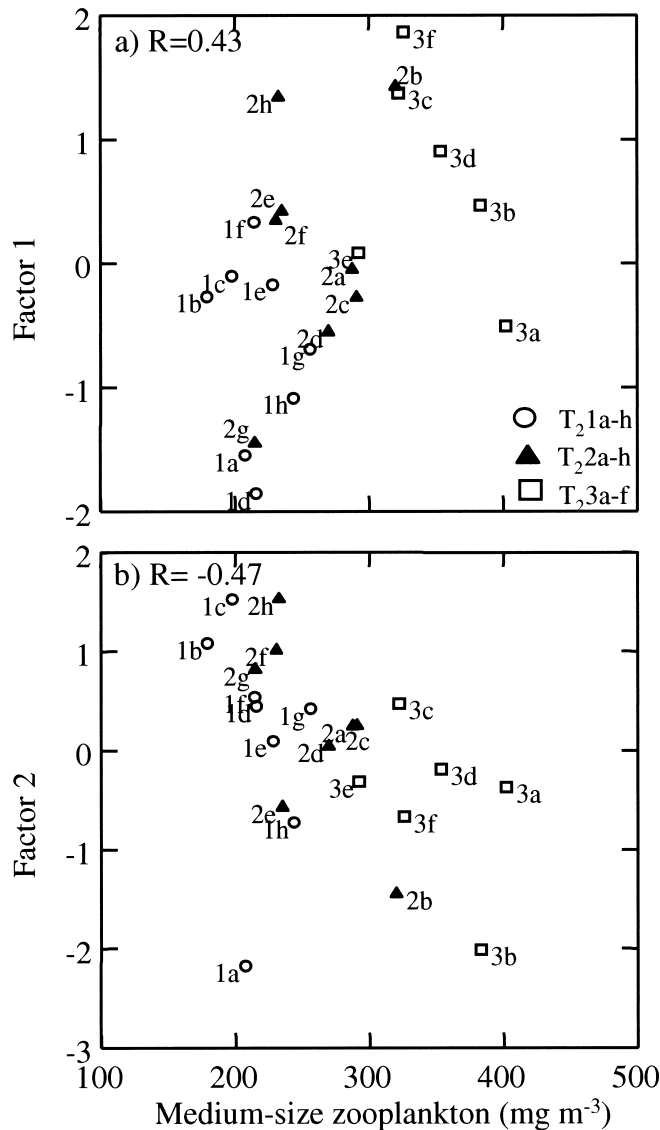


Fig. 12. Scattergram of the relationship between (a) larval fish PCA factor 1 and (b) factor 2 and medium-sized (764–1,003- $\mu\text{m}$  ESD) zooplankton biomass concentration ( $\text{mg m}^{-3}$ ). Each datum is identified by transect number and neuston net, as in Table 1.

T<sub>2</sub>2b, T<sub>2</sub>3a, and T<sub>2</sub>3e), which corresponded to samples of low or high medium-sized zooplankton biomass, respectively. Particles that we classified as “small” were composed of detritus, invertebrate eggs, the cyclopoid copepod *Oithona* (1% of particles examined), and calanoids *Acartia* (3%), *Calanopia* (3%), *Tortanus* (2%), *Undinula* (20%), and the smaller developmental stages of other copepods (Table 2). Detritus (17%) was usually composed of algal slime and fibrous material and was <1,500- $\mu\text{m}$  ESD on T<sub>2</sub>1 and <4,005- $\mu\text{m}$  ESD on T<sub>2</sub>2 and T<sub>2</sub>3. Medium-sized particles were composed of larger detritus (including grains of sediment), *Sagitta* (8%), the calanoids *Eucalanus* (10%) and *Labidocera* (2%), a euphausiid (3%, *Nyctiphanes* sp.), a carid shrimp (6%, Pasiphaeidae), and decapods (3%) (Table 2). Rarer crustaceans included the epipelagic synopiid amphipod *Synopia ultramarina* Dana 1853 (Barnard and Karaman

1991) and those more typically associated with the benthos such as an ostracod and a carid shrimp, which were found more frequently in the neuston samples collected along T<sub>2</sub>3, when light attenuation was higher.

## Discussion

The flood tide wake in the lee of Derwent Island revealed a pattern of flow disturbance that is typically observed in the lee of other islands in shallow seas (Pattiaratchi et al. 1986). Flood tide flows were typically 0.5–1.0  $\text{m s}^{-1}$ , with some evidence of a pair of lee eddies centered near 149.775°W, 21.00°S and at 149.795°W, 21.01°S. There was evidence of high light attenuation (evidence of upwelling of fine sediments) at some locations, accompanied by variation in the zooplankton particle-size field. The processes of EU and EA can be assessed with our data, acknowledging that there are other complicating effects of small reefs on the horizontal turbulence (Middleton et al. 1993) and stochastic variation in the upstream flow (Aiken et al. 2002). The oscillatory nature of the incident tidal current provides a strong constraint on the wake development (Black and Gay 1986). This precludes any comparison with the traditional wake structures caused by steady incident flows such as the von Karman vortex street or the formation of steady recirculating eddies (Denniss and Middleton 1994; Chen and Jirka 1995).

*EU*—Boundary-layer fluid is driven along the seabed below an eddy toward the rotation axis and then toward the surface (Greenspan 1968; Schlichting 1968). The process involves a coupling between flow in the frictional bottom-boundary layer and inviscid flow above. In the inviscid region, the centripetal acceleration in a rotating flow tends to be balanced by the pressure-gradient forces. The latter arise from deformations of the sea surface, with sea level being lower at the eddy center. This pressure gradient extends to the bottom boundary layer, where circumferential velocities decrease and shears increase and where frictional forces contribute to a locally steady balance. As a consequence, boundary-layer flow is driven by the pressure gradient toward the axis of rotation. The resultant convergence yields upward flow that may transport sediments and bottom-preferential species toward the surface. For a pair of steady lee eddies, we would predict two local maxima in the near-surface concentration of such substances (Fig. 1a).

The upwelling velocity scale,  $W_e$ , can be estimated (Garrett and Loucks 1976) by noting that the boundary layer balance between the pressure-gradient force and frictional stress yields  $V_e^2/R_e \sim C_D U_e V_e/h$ , where  $V_e$  is the azimuthal component of eddy velocity above the boundary layer,  $R_e$  is the eddy radius,  $C_D$  is the drag coefficient for a quadratic drag law, and  $U_e$  is the inward velocity within a bottom boundary layer of height  $h$ , assumed to be less than  $H$ , the water depth. Thus, a scale for the inward radial transport in the bottom boundary layer is  $2\pi R_e U_e h$ . Balancing this transport by upwelling through the plan area  $\pi R_e^2$  thus yields an upwelling velocity  $W_e \sim 2U_e h/R_e$ . It follows that

$$W_e = 2V_e h^2 / (C_D R_e^2) \quad (1)$$

is a scale for the upwelling speed within eddies. For the

present application, we chose scales of  $V_e = 0.5 \text{ m s}^{-1}$ ,  $R_e = 10^3 \text{ m}$ , and  $C_D = 3 \times 10^{-3}$  (Sleath 1984). The boundary layer has not been measured but was not evident in the ADCP data and was therefore smaller than the unresolved bottom current thickness. We chose  $h = 1 \text{ m}$  as a suitable scale, which yielded an upwelling velocity of  $3 \times 10^{-4} \text{ m s}^{-1}$ , consistent with the still water (Stokes) sinking rate of quartz sediment particles of diameter  $20 \mu\text{m}$  (Sleath 1984). Particle Reynolds numbers computed from Stokes settling formula were  $<1$ ; thus, the Stokes settling law was valid for these small particles. Our findings are compared with EA in the next section.

**EA**—Flow diverted around an island is intensified at the island flanks, increasing the erosion of sediments in that region and the rate of vertical mixing, including the entrainment of demersal and benthic species toward the surface. The horseshoe vortex generated initially in the boundary layer at the seabed becomes part of the turbulent horizontal shear layer almost immediately on separation from the island (Thwaites 1960). The combination of strong shear and vorticity mixes particles throughout the entire water column immediately downstream of the island, which is why we denote this as the EA process.

A criterion for sediment erosion is provided by focusing on the Shields parameter  $\theta = \tau/(gd\Delta\rho)$ , where  $\tau$  is the bottom stress,  $\Delta\rho$  is the density contrast between the sediment and the fluid,  $g$  is the acceleration due to gravity, and  $d$  is the diameter of the sediment particles (Raudkivi 1976; Sleath 1984). Measurements suggest that sediment erosion occurs only if  $\theta$  exceeds a critical value,  $\theta_c$ , of order 1.0. Thus, we can predict that sediment will be eroded from the bottom near the island only if its particle diameter  $d < d_c$ , where  $d_c$  is a critical diameter defined by

$$d_c < C_D U_i^2 / (g\theta_c \Delta\rho/\rho_0) \quad (2)$$

where  $U_i$  is the near-island water speed and  $\rho_0$  is the water density. For sediments sinking at a rate  $w$ , the downstream length scale for the surface layer manifestation of a sediment plume is

$$L_p = U_i \Delta z / w, \quad (3)$$

where  $\Delta z$  is the thickness of the surface layer under consideration (e.g., that visible from an airplane). This scale assumes steady flow and will thus be superseded by the tidal ellipse, if that is smaller. As for the plume geometry, it may take the form of two isolated plumes or it may form a full, or partial, V-shape pattern or even a Y-shape pattern, according to whether particles leave the surface zone before the particles in the streamlines converge (Fig. 1b). In the present application, assuming that the bottom sediments have a relative density contrast  $\Delta\rho/\rho_0 = 1.6$ , as is the case for quartz (Sleath 1984), and with velocities  $U_i = 1 \text{ m s}^{-1}$ , we estimate the diameter of eroding sediments to be  $d_c < 200 \pm 65 \mu\text{m}$  (Eq. 2). With  $\Delta z = 15 \text{ m}$  and under the assumption of  $200\text{-}\mu\text{m}$  quartz particles with turbulent sinking rates  $40 \pm 20\%$  of the still-water sinking rates (Murray 1970; Nielson 1993), we estimate the downstream scale of the EA plume to be  $0.8 \text{ km}$  (to within a factor of 2). This is roughly comparable to the geometric mean island diam-

eter, which implies that sediments will remain suspended within an island scale distance downstream, as observed in Fig. 7.

**EU and EA of epibenthic material**—At maximal upwelling velocities of  $0.3 \text{ mm s}^{-1}$  for the EU process, the finer sediments would take  $>1 \text{ d}$  to reach the surface at local depths. Because this period exceeds the tidal period, we can conclude that the EU process will not yield observable patches of surface concentration (Fig. 1a). By contrast, we have several types of evidence consistent with the EA process. There is a V-shaped plume of increased light attenuation that contains a region of low attenuation immediately downstream (at least during  $T_{11}$  and  $T_{12}$ ). The V-shaped plume begins  $<1 \text{ km}$  downstream and  $<1 \text{ km}$  beyond the eastern and western flanks of the island on  $T_{11}$ . By the time transect  $T_{12}$  was completed, time and distance had permitted vertical mixing to increase light attenuation (at the western end of  $T_{12}$ ), and the plume appeared to be closer to the wake center. On transects  $T_{13}$  and  $T_{14}$ , the apex of the V-shape was apparent. The downstream extent of sinking sedimentary particles  $135\text{--}265 \mu\text{m}$  in diameter is estimated to be between  $0.4$  to  $2 \text{ km}$ , consistent with the observed pattern (Figs. 6, 7a, 8a).

Our interpretation of the three-dimensional flow of silt and zooplankton is consistent with the observed upstream conditions at Derwent (Fig. 11), where light attenuation was  $<1,850$  overall and was highest near the bottom along with the medium-sized zooplankton biomass. Downstream, we observed the ascending column of elevated light attenuation in the vertical profiles over the three transects on the second night, despite flow being slower than it had been on the previous night. Increased mixing could overcome the swimming speed of small zooplankton and deplete their surface abundance while increasing light attenuation (Fig. 13). We did not sample water of high attenuation for sediment size, but we did observe grains in the neuston net collection of the second night, along with taxa known to be epibenthic, including a carid shrimp, an ostracod, and some larval fish (see below). Indeed, nearly 20% of the particles we examined in the neuston net collections were detritus—mostly plant debris—which increased from  $500\text{-}\mu\text{m}$  ESD (the average ESD of the largest particles in  $T_{21}$  samples) to  $>2,000\text{-}\mu\text{m}$  ESD by  $T_{22}$  and  $T_{23}$ . During  $T_{22}$  and  $T_{23}$ , we observed similar species, along with amphipods (*Synopia*), larval decapods, small gastropods, and bivalves indicative of an epibenthic origin.

Sediments in the vicinity of Rattray Island ( $20^\circ\text{S}$ ,  $149.5^\circ\text{E}$ ), which is also within the Whitsunday Island group, were reported to be 61–75% silt ( $3\text{--}62 \mu\text{m}$ ; Wolanski et al. 1984a). Settling rates of  $3\text{--}62\text{-}\mu\text{m}$  diameter quartz particles, as indicated by Stokes' Law, are  $2\text{--}3 \text{ m h}^{-1}$  and are of sufficient magnitude to explain the observed decline in light attenuation. Deep scour holes are reported in the region where island flanks are aligned normal to the incident flow (Wolanski et al. 1984a; Furukawa and Wolanski 1998) and where coarse shell fragments are found on the seabed. Similar scour holes would be expected near the flanks of Derwent Island.

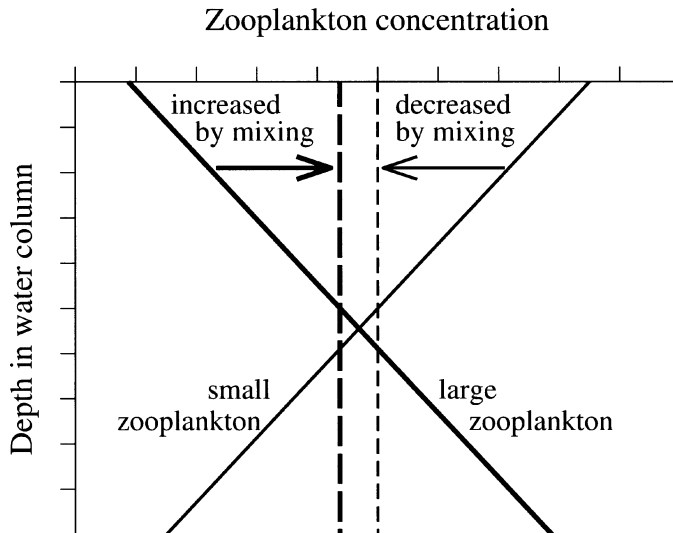


Fig. 13. Definition sketch explaining how vertical mixing might lead to a decrease in the surface concentration of small zooplankton, which would otherwise be concentrated near the surface, while at the same time leading to an increase in the surface concentration of sediments and larger demersal zooplankton. The diagonal lines represent the initial concentration profiles, and the dashed vertical lines represent the result of homogenization caused by mixing.

*Distribution of larval fish*—The first two principal components of the 11 abundant taxa of neustonic larval fish were in one case negatively, and the other positively, correlated with the biomass of medium-sized zooplankton. Larval bregmacerotids (or “codlets”), gobies, carangids, leiognathids, platycephalids, and priacanthids that grouped in factor 1 were significantly correlated with the biomass of bottom-associated medium-sized zooplankton. Overall, the abundance of the first group of larvae increased from transect  $T_21$  to  $T_23$ , whereas the second group decreased during the passage of the flood tide. Larval gerreids, bothids, and nemipterids in factor 2 were negatively correlated with medium-sized zooplankton; thus, the uplifting of bottom water could also displace this larval community, along with the small zooplankton biomass.

There have been few studies on the vertical distribution of larval tropical fish to help interpret these data (e.g., Leis 1991). Synodontids (lizardfishes) are the one taxon reported to persist in deeper water (13–20 m) both day and night (Leis 1991), yet we found no relationship of this taxon with any other, nor with any OPC data. The larval bregmacerotids found in our study may be considered to be typical of deeper water (Matsuura et al. 1993) and, after being stirred to the surface, would be concentrated downstream, as shown in Fig. 7c. Bregmacerotids, which as adults are small, <120-mm maximum length tropical gadiforms, are a common component of tropical oceanic ichthyoplankton. *Bregmaceros mccllellandi*, *Bregmaceros nectabanus*, and *Bregmaceros rarisquamosus* are recorded from Queensland coastal waters (M. McGrouther, Australian Museum, pers. comm.). Two species of larval bregmacerotids on the shelf off Brazil (*Bregmaceros cantori* and *Bregmaceros atlanticus*), between

23°S and 30°S were found in deeper water >40 m and rarely penetrated the upper 30 m at night (Matsuura et al. 1993).

We tested the OPC’s estimates of size and abundance with the neustonic abundance of larval fish: that is, does the size and concentration of larval fish approximate that estimated by extrapolating the OPC’s abundance-at-size distribution? Most larval fish we observed ranged in length between 5 and 10 mm, with a body depth of 1–2 mm, which is approximately equivalent to a maximum possible ESD between 2,500–5,000  $\mu\text{m}$ . The OPC’s estimate of the mean abundance of particles in only two size categories corresponding to the smallest fish larvae (geometric mean size of 2,429- and 2,566- $\mu\text{m}$  ESD), at OPC depths shallower than 10 m during all the neuston tows, was  $0.61\text{ m}^{-3}$ , compared with the average neuston catch of  $1.40\text{ m}^{-3}$ . A difference of ~50% is relatively small, considering our use of only two OPC size categories for larval fish, the possible gear avoidance of the OPC by larvae, and the depth and volume differences between the neuston net and the OPC.

In conclusion, we met the challenges of examining the small-scale dynamics of an island wake by frequent sampling with a neuston net and with high-frequency sampling of the OPC and ADCP. Nevertheless, our study was aliased in time and space and much of our analysis of wake dynamics is inferred. Despite this shortcoming, our study indicates there are dynamic physical and biological processes that can explain much of the structure of flow disturbance, patterns of light attenuation, zooplankton size structure and abundance, and the abundance and species composition of ichthyoplankton.

We examined two physical processes in the study. EU had limited influence, whereas EA dominated the wake, producing a V-shaped plume and a patch of distinctive zooplankton downstream (Fig. 1). In shallow and tidally energetic regions, EA may generally be more common than EU. We found that, at the end of the nighttime flood tide, high concentrations of medium-sized zooplankton and larval fish were observed 1–2 island diameters downstream. The fate of this patch is unknown, but it would presumably be advected in a manner consistent with the tidal ellipse. If the trajectory of this ellipse intersects with locally suitable habitats (e.g., a reef), then the EA associated with island wakes could provide another explanation for generating locally enhanced larval settlement or “recruitment hotspots” (Sammarco and Andrews 1988, 1989; Kingsford et al. 1991; McNiell et al. 1992). Our study has wider implications for predicting recruitment hotspots in general, by locating the regionally appropriate tidal excursion onto the observed sediment plumes, such as those seen in the Great Barrier Reef (e.g., Wolanski et al. 1984a,b). The intersection of the tidal excursion and suitable habitat could then be sampled and compared with other sites to test this prediction.

## References

- AIKEN, C. M., A. M. MOORE, AND J. H. MIDDLETON. 2002. The non-normality of coastal ocean flows around obstacles, and their response to stochastic forcing, *J. Phys. Oceanogr.* **32**: 2955–2974.
- ALLDREDGE, A. L., AND W. M. HAMNER. 1980. Recurring aggre-

- gation of zooplankton by a tidal current. *Estuar. Coast. Mar. Sci.* **10**: 31–37.
- BARNARD, J. L., AND K. S. KARAMAN. 1991. Marine gammaridean Amphipoda: Records of the Australian Museum, supplement 13, part 2. Australian Museum.
- BLACK, K., AND S. GAY. 1986. Eddy formation in unsteady flows. *J. Geophys. Res.* **92**: 9514–9522.
- CHEN, D., AND G. H. JIRKA. 1995. Experimental study of plane turbulent wakes in a shallow water layer. *Fluid Dyn. Res.* **16**: 11–41.
- DENNISS, T., AND J. H. MIDDLETON. 1994. Effects of viscosity and bottom friction on recirculating flows. *J. Geophys. Res.* **99**: 10183–10192.
- FURAKAWA, K., AND E. WOLANSKI. 1998. Shallow water frictional effects in island wakes. *Estuar. Coast. Shelf Sci.* **46**: 599–608.
- GARRETT, C., AND R. LOUCKS. 1976. Upwelling along the Yarmouth shore of Nova Scotia. *J. Fish. Res. Bd. Can.* **33**: 116–117.
- GREENSPAN, H. P. 1968. The theory of rotating fluids. Cambridge Univ. Press.
- HAMNER, W. M., AND I. R. HAURI. 1977. Fine-scale surface currents in the Whitsunday Islands, Queensland Australia: Effect of tide and topography. *Aust. J. Mar. Freshw. Res.* **28**: 333–359.
- , AND ———. 1981. Effects of island mass: Water flow and plankton pattern around a reef in the Great Barrier Reef lagoon, Australia. *Limnol. Oceanogr.* **26**: 1084–1102.
- HERMAN, A. W. 1988. Simultaneous measurements of zooplankton and light attenuation with a new optical plankton counter. *Cont. Shelf Res.* **8**: 205–221.
- HOPCROFT, R. 2002. Comparison of plankton size spectra from net tow samples and OPC measurements in marine waters, p. 7–11. *In* M. Zhou and K. Tande [eds.], *Optical Plankton Counter Workshop*. GLOBEC report 17. GLOBEC International Project Office.
- HUNTLEY, M. E., M. ZHOU, AND W. NORDHAUSEN. 1995. Mesoscale distribution of zooplankton in the California current in late spring, observed by an OPC. *J. Mar. Res.* **53**: 647–674.
- KINGSFORD, M. J., AND I. M. SUTHERS. 1996. The influence of the tide on patterns of ichthyoplankton abundance in the vicinity of an estuarine front, Botany Bay, Australia. *Estuar. Coast. Shelf Sci.* **43**: 33–54.
- , E. WOLANSKI, AND J. H. CHOAT. 1991. Influence of tidally induced fronts and Langmuir circulations on distribution and movements of presettlement fishes around a coral reef. *Mar. Biol.* **109**: 167–180.
- LEGENDRE, P., AND L. LEGENDRE. 1998. *Numerical ecology*, 2nd ed. Developments in environmental modeling 20. Elsevier Science.
- LEIS, J. M. 1991. Vertical distribution of fish larvae in the Great Barrier Reef lagoon, Australia. *Mar. Biol.* **106**: 1–10.
- , AND D. RENNIS. 1983. The larvae of Indo-Pacific coral reef fishes. New South Wales Univ. Press.
- , AND T. TRINSKI. 1989. The larvae of Indo-Pacific shore-fishes. New South Wales Univ. Press.
- LEVI, E. 1995. The science of water: The foundation of modern hydraulics. ASCE Press.
- MATSUURA, Y., A. C. DE SILVA GARCIA, M. KATSURAGAWA, AND K. SUZUKI. 1993. Distribution and abundance of two species of codlet Teleostei, Bregmacerotidae larvae from the south-eastern Brazilian Bight. *Fish. Oceanogr.* **2**: 82–90.
- MCNEILL, S. E., D. G. WORTHINGTON, D. J. FERRELL, AND J. D. BELL. 1992. Consistently outstanding recruitment of five species of fish to a seagrass bed in Botany Bay, NSW. *Aust. J. Ecol.* **17**: 359–365.
- MIDDLETON, J. H., V. T. BUCHWALD, AND J. M. HUTHNANCE. 1984. The anomalous tides near Broad Sound. *Cont. Shelf Res.* **3**: 359–381.
- , D. A. GRIFFIN, AND A. M. MOORE. 1993. Oceanic circulation and turbulence in the coastal zone. *Cont. Shelf Res.* **13**: 143–168.
- MURDOCH, R. C., R. PROCTOR, J. B. JILLET, AND J. R. ZELDIS. 1990. Evidence for an eddy over the continental shelf in the downstream lee of Otago Peninsula, New Zealand. *Estuar. Coast. Shelf Sci.* **30**: 489–507.
- MURRAY, S. P. 1970. Settling velocity and vertical diffusion of particles in turbulent water. *J. Geophys. Res.* **75**: 1647–1654.
- NIELSEN, P. 1993. Turbulence effects on the settling of suspended particles. *J. Sediment. Petrol.* **63**: 835–838.
- PATTIARATCHI, C., A. JAMES, AND M. COLLINS. 1986. Island wakes and headland eddies: A comparison between remotely sensed data and laboratory experiments. *J. Geophys. Res.* **92**: 783–794.
- RAUDKIVI, A. J. 1976. *Loose boundary hydraulics*. Pergamon.
- RISSIK, D., I. M. SUTHERS, AND C. T. TAGGART. 1997. Enhanced zooplankton abundance in the lee of an isolated reef in the south Coral Sea: The role of flow disturbance. *J. Plankton Res.* **19**: 1347–1368.
- SAMMARCO, P., AND J. ANDREWS. 1988. Localised dispersal and recruitment in Great Barrier Reef corals: The Helix experiment. *Science* **239**: 1422–1424.
- , AND ———. 1989. The Helix experiment: Differential localised dispersal and recruitment patterns in Great Barrier Reef corals. *Limnol. Oceanogr.* **34**: 896–912.
- SCHLICHTING, H. 1968. *Boundary layer theory*. McGraw-Hill.
- SIGNELL, R. P., AND W. R. GEYER. 1991. Transient eddy formation around headlands. *J. Geophys. Res.* **96**: 2561–2575.
- SLEATH, J. F. A. 1984. *Sea bed mechanics*. Wiley.
- SPRULES, W., AND OTHERS. 1992. Non-video optical instruments for studying zooplankton distribution and abundance. *Arch. Hydrobiol. Beih.* **36**: 45–58.
- TAGGART, C. T., K. R. THOMPSON, G. L. MAILLET, S. E. LOCHMAN, AND D. A. GRIFFIN. 1996. Abundance distribution of larval cod *Gadus morhua* and zooplankton in a gyre-like water mass on the Scotian Shelf, p. 155–173. *In* Y. Watanabe, Y. Yamashita, and Y. Oozeki [eds.], *Survival strategies in early life stages of marine resources*. A. A. Balkema.
- THWAITES, B. 1960. *Incompressible aerodynamics*. Oxford Univ. Press.
- TOWNSEND, D., C. YENTSCH, C. PARKER, W. BALCH, AND E. TRUE. 1983. An island mixing effect in the coastal Gulf of Maine. *Helgol. Meeresunters.* **36**: 347–356.
- WOLANSKI, E., J. IMBERGER, AND M. L. HERON. 1984a. Island wakes in shallow coastal waters. *J. Geophys. Res.* **89**: 10553–10569.
- , G. PICKARD, AND D. L. B. JUPP. 1984b. River plumes, coral reefs and mixing in the Gulf of Papua and the northern Great Barrier Reef. *Estuar. Coast. Shelf Sci.* **18**: 291–314.

Received: 10 January 2003

Accepted: 5 August 2003

Amended: 23 September 2003